Received: 21 November 2021 | Revised: 1 March 2022 | Accepted: 9 March 2022

DOI: 10.1111/jace.18458

Journal of the American Ceramic Society

RESEARCH ARTICLE

Profiling hot isostatically pressed canister–wasteform interaction for Pu-bearing zirconolite-rich wasteforms

Pranesh Dayal | **Rifat Farzana** | **Yingjie Zhang** | **Gregory R. Lumpkin** | **Rohan Holmes** | **Gerry Triani** | **Daniel J. Gregg**

Australian Nuclear Science and Technology Organisation, Kirrawee DC, New South Wales, Australia

Correspondence
Daniel J. Gregg, Australian Nuclear Science and Technology Organisation, Locked Bag 2001, Kirrawee DC, NSW 2232, Australia.
Email: dgg@ansto.gov.au

Funding information
Nuclear Decommissioning Authority, United Kingdom

Abstract

Zirconolite-rich full ceramic wasteforms designed to immobilize Pu-bearing wastes were produced via hot isostatic pressing (HIP) using stainless steel (SS) and nickel (Ni) HIP canisters. A detailed profiling of the elemental compositions of the major and minor phases over the canister–wasteform interaction zone was performed using scanning electron microscopy combined with energy-dispersive X-ray spectroscopy (SEM-EDS) characterization. Bulk sample analyses from regions near the center of the HIP canister were also conducted for both samples using X-ray diffraction and SEM-EDS. The sample with the Ni HIP canister showed almost no interaction zone with only minor diffusion of Ni from the inner wall of the canister into the near-surface region of the wasteform. The sample with the SS HIP canister showed ~100–120 μm of interaction zone dominated by high-temperature Cr diffusion from canister materials to the wasteform with the Cr predominantly incorporated into the durable zirconolite phase. We also examined, for the first time, changes to the HIP canister wall thickness caused by HIPing and demonstrated that no canister wall thinning occurred. Instead, in the areas examined, the canister wall thickness was observed to increase (up to ~20%) due to the compression occurring during the HIP cycle. Further, only sparse formation of (Cr, Mn)-rich oxide particles were noted within the HIP canister inner wall area immediately adjacent to the ceramic material, with no evidence for reverse diffusion of ceramic materials. Though the HIP canister–wasteform interaction extends to ~120 μm when using an SS HIP canister for the system investigated, this translates to <<1 vol.% for an industrial scale HIPed wasteform. Importantly, the HIP canister–wasteform interactions did not produce any obviously less durable phases in the wasteform or had any detrimental impact on the HIP canister properties.

KEYWORDS
hot isostatic pressing, interfaces, Pu-bearing nuclear waste, radioactive waste, Synroc

1 | INTRODUCTION

Nuclear waste disposal has been an important and complex issue for the nuclear industry since the development of nuclear power from the 1940s onward. Of particular, the concern is plutonium that is generated in nuclear reactors by neutron capture during the irradiation of the uranium in nuclear fuel.[1,2] The hazard associated with nuclear waste depends on the radioactivity level and nature of the radionuclide, and appropriate immobilization is required to prevent radionuclide release to the biosphere during final disposal in a repository.[3] Most plutonium isotopes exhibit a significant radiotoxicity hazard and half-lives that are several thousands to hundreds of thousands of years, thus requiring long-term immobilization and geological disposal when a nuclear waste is considered.[2] As per the International Atomic Energy Agency, immobilization is the conversion of a waste into a wasteform by solidification, within which the radionuclides are incorporated within the matrix or encapsulated. Several classes of wasteform are generally accepted for the range of waste types that exist globally, such as cement-, glass-, glass–ceramic (GC)-, and ceramic-based wasteforms, the choice of which being dependent on the waste to be treated and the regulatory performance criteria.[3,4] Though the wasteform primarily ensures the structural stability and associated performance, conditioning refers to those engineering operations that render the wasteform suitable for handling, transportation, storage, and disposal.[3] The commonly accepted baseline waste immobilization technology for intermediate- and high-level radioactive wastes is vitrification into a borosilicate glass wasteform.[5] Since 1979, a multiphase ceramic wasteform called Synroc[6] and its derivatives have gained significant attention as potential candidates for the immobilization of challenging radioactive wastes. The resulting Synroc-type wasteform exhibits better performance than conventional glass wasteforms from an aqueous durability perspective.[7] The particular emphasis currently for the utility of Synroc is on wastes that are problematic for glass matrices or existing vitrification process technologies, of which plutonium bearing wastes are a notable example.[8] Further, Synroc has developed into a technology platform using hot isostatic pressing (HIP) as the processing method to consolidate the waste and tailored additives into a dense, highly durable wasteform.[4]

The Australian Nuclear Science and Technology Organisation is currently building a Synroc Waste Treatment Facility for its Mo-99 production wastes, and this will achieve a first-of-a-kind industrial demonstration of the HIP technology for nuclear wastes.[9,10] HIP is an attractive processing option for the consolidation of radioactive waste with the ability to process a wide range of waste streams, targeting minimal secondary waste generation and minimal volatile losses during processing.[4,11] HIPed wasteforms have been demonstrated for a variety of problematic wastes, for example, uranium-rich radioactive wastes arising from Mo-99 production,[12,13] radioiodine from the PUREX process,[14] and fluoride molten salt wastes.[15] These wasteforms produced by HIPing can be either full ceramic (C), GC, or glass (G) and are tailored to the waste stream chemistry. For the management of Pu-bearing waste material, leading candidates currently being considered are zirconolite- or pyrochlore-based full C wasteforms or GC wasteforms, fabricated by HIPing.[8,16,17]

Zirconolite (general formula, $CaZrTi_2O_7$) is one of the key mineral phases in the original titanate-based Synroc formulation and has long been accepted as a radiation-tolerant and chemically durable phase to host actinides, such as U, Np, and Pu.[7,18–20] In zirconolite, Ca- and Zr cations are eight- and sevenfold coordinated, respectively. There are three unique Ti coordination polyhedra, encompassing two fully occupied octahedral sites (TiO_6 polyhedra) and 0.5 occupancies at trigonal bipyramidal (TiO_5) site.[20] Trivalent and tetravalent early actinide ions can be incorporated on either the Ca or Zr site.[4] Zirconolite is known to have various polytypes like zirconolite-2M, 3T, 4M according to the structural transitions with increased lattice substitutions and synthesis conditions.[21] The ideal zirconolite comprises planes of corner and edge sharing CaO_8 and ZrO_7 polyhedra, interleaved by hexagonal tungsten bronze (HTB) type Ti–O layers along (001) and is referred to as zirconolite-2M. The zirconolite polytypes are then characterized by the variation in a stacking sequence of adjacent Ca/Zr and HTB-type Ti–O layers.[20] A cubic pyrochlore structure is produced when high levels of actinide (such as Pu) and REE are incorporated.[21,22] Pyrochlore has the general formula of $A_2B_2X_6Y$ and is a derivative of the fluorite structure. In pyrochlore, A is an eight-coordinated and B is a six-coordinated cation site that can incorporate mono- to hexavalent and tri- to hexavalent cations, respectively. X and Y are four-coordinated anion sites.[5]

At HIPing conditions (high temperatures and high pressures), the Pu-bearing zirconolite-rich wasteform and the metallic HIP canister used for containment of the waste material during HIPing can potentially interact.[16] This interaction may produce phases that are different to the targeted bulk wasteform material or possibly with different chemical compositions to that of the bulk, due to the potential for elemental diffusion across the canister–wasteform interface.[16] Also, recent studies by Guo et al.[23] highlighted the possibility of localized corrosion at the interfaces between canister materials and wasteforms. The severity of this interfacial corrosion may depend on the

type of phase(s) present at the canister–wasteform interface. Therefore, it is essential to understand the overall effect of the HIP canister–wasteform interaction on both the canister and the targeted wasteform composition.

The previous work reported the interaction of a stainless steel (SS) HIP canister with a zirconolite-rich Synroc formulation and with Ce incorporated as an actinide simulant.[16] Following this Ce surrogate work, a U/Th- and Pu-validation study[7] was also undertaken in which the zirconolite-based wasteform was similarly HIPed in SS using the same conditions. In all cases, the interaction zone was divided into distinct layers, and these layers were Cr-depleted SS with Cr-oxide inclusions, a Cr/Fe-oxide front that was derived from diffusion and oxidation of Cr and Fe out of SS, and a modified wasteform area. Scanning electron microscopy combined with energy-dispersive X-ray spectroscopy (SEM-EDS) analysis detected small amounts of Cr or Fe as far as 500 μm into the wasteform, with Fe generally appearing to be more mobile. Recently, the interaction of an SS HIP canister with zirconolite[24] (nominal composition $Ca_{0.80}Ce_{0.20}ZrTi_{1.60}Cr_{0.40}O_7$ using Cr^{3+} as a charge compensator) was inspected following HIPing. This study[24] observed, 5–8 μm of interaction region dominated by a Cr-rich oxide layer and reported that minor Cr or Fe diffusion did not significantly destabilize the phase assemblage at the canister–ceramic wasteform interface. However, the analyses described in the works earlier were undertaken focusing predominantly on the SS HIP canister material and using EDS line-scans/mapping rather than providing a detailed profile of the elemental distribution within the interaction zone.

The SS canister–wasteform interaction was similarly investigated for a pyrochlore-rich formulation produced by HIPing[17] and using U as a surrogate for Pu. An analogous sequence to that for the zirconolite system was noted at the canister wasteform interaction; however, in the case of pyrochlore, Fe and Cr migration appeared limited. Instead, the diffusion of Fe/Cr from the SS and Al/Ti from the wasteform (from hollandite and rutile) resulted in the formation of mixed oxide solid solutions in the interface region.

Ceramic systems other than titanates have also been consolidated via HIPing. Iodosodalite, for example, is a candidate ceramic wasteform for the immobilization of iodine wastes from the fuel cycle and was produced by HIPing using a variety of HIP canister materials, including Fe, Ni, and Cu[16] . In that study, the canister–wasteform interaction was diverse and appeared to be dependent on more than just the canister materials' relative positions on the electrochemical scale. It was therefore postulated that the extent of interaction with the HIP canister was the result of a combination of several factors such as reduction potential for the HIP canister material, the formation of a "protective" oxide layer on the canister internal wall and HIP consolidation conditions, particularly temperature. With regards to temperature, it was not necessarily the absolute temperature, but also closeness to the melting point of the HIP canister material that promoted atomic mobilities from the metal. To the best of the author's knowledge, the previous details summarize the results from published studies investigating the HIP canister–ceramic wasteform interaction zone. Interaction studies involving Pu-bearing wasteforms with different canister materials are therefore limited. Moreover, those HIP canister–wasteform interaction studies currently published largely overlook the impact on HIP canister wall thickness and do not provide a detailed elemental profiling through the interaction zone.

In this study, zirconolite-rich full ceramic wasteforms designed to immobilize Pu-bearing wastes were produced via HIPing using SS and nickel (Ni) HIP canisters. Though the work described is not exactly a systematic study, the difficulty in handling Pu-bearing material and the significant cost, as well as safety and regulatory requirements often limit such work. For the first time, this study reports a detailed profiling of the elemental compositions of the major (zirconolite) and minor phases over the interaction zone with SS and Ni HIP canisters for Pu-bearing materials. We also examine the changes to the HIP canister wall thickness, porosity, and phase composition at the interface, as influenced by the HIP canister material itself and the wasteform chemistry.

2 | EXPERIMENTAL PROCEDURE

2.1 | Sample preparation

Two HIPed Pu-bearing zirconolite rich ceramic formulations were prepared and are designated HIP-SS and HIP-Ni. In this nomenclature, "SS" or "Ni" indicates the HIP canister material. The oxide compositions for both Pu-bearing samples are provided in Table 1. Further details for each formulation are as follows:

HIP-SS: The Pu-doped sample was designed to form 80 wt.% of zirconolite (containing Gd, Sm, and Hf as neutron poisons), with ~10 wt.% each of Ba-hollandite (nominally $BaAl_2Ti_6O_{16}$) and rutile (nominally TiO_2). The wasteform contained 13.5 wt.% PuO_2 as well as 10 wt.% HfO_2, 4.2 wt.% Gd_2O_3, and 4.2 wt.% Sm_2O_3. In the wasteform design, Pu was expected to be shared between the Ca- and Zr sites, whereas Gd and Sm were expected to be largely confined to the Ca site with Hf predominantly on the Zr site. Hollandite was incorporated into the wasteform design as a possible host phase for radioactive Cs (though no inactive or active Cs was incorporated in the current study), as a potential internal gamma radiation

TABLE 1 Oxide compositions (wt.%) of the Pu-bearing samples[a]

Oxide	HIP-SS	HIP-Ni
Al_2O_3	6.9	0.3
BaO	2.3	–
CaO	5.9	11.9
TiO_2	40.1	41.2
ZrO_2	13.0	10.2
Gd_2O_3	4.2	6.4
Sm_2O_3	4.2	–
HfO_2	10.0	–
ThO_2	–	3.0
UO_2	–	12.0
PuO_2	13.5	15.0
Total	**100**	**100**

[a]SS = stainless steel HIP canister, Ni = nickel metal HIP canister.

shield to reduce the risk of future plutonium diversion. In addition, the inclusion of hollandite and rutile provides a multiphase system to provide some flexibility to potential waste variations and to permit the formation of fine grained (~1 μm) microstructures through the avoidance of grain growth.

The sample was prepared (20 g) via the alkoxide route in which the Pu was introduced as a nitrate solution prior to calcination at 750°C in argon for 1 h. The calcined powder was then ball milled, dried, and loaded into an SS HIP canister. The HIP canister was evacuated and sealed and HIPed (AIP 6 30H) at 1280°C and at 150 MPa for 2.5 h. The wasteform design is similar to that produced by Zhang et al.[7]; however, the current sample was designed to replace half of the Gd with Sm. The idea was to examine the effect of mixed neutron absorbers on the overall wasteform phase assemblage. From a processing perspective, the current study also employs a marginally shorter HIP processing time as compared to that of Zhang et al.[7] A sample was cut from the HIPed ceramic adjoining the SS canister with special care to prevent delamination. The sample was then cross-sectionally mounted in epoxy resin and polished to a 1-μm diamond finish for SEM analysis. A sample of the ceramic was extracted from the center of the SS canister and similarly mounted in epoxy resin and polished flat for X-ray diffraction (XRD) analysis.

HIP-Ni: The Pu-doped sample was designed to form pyrochlore, plus ~25% zirconolite and minor rutile. The wasteform contained 15 wt.% PuO_2–6 wt.% Gd_2O_3. In the wasteform design, Pu and Gd were expected to be partitioned between the pyrochlore and zirconolite phases. The sample was prepared (13 g) via the oxide route in which all actinides were introduced as oxides (U_3O_8, ThO_2, and PuO_2, representing mixed actinide material). The powder mixture was calcined at 750°C for 1 h in air and then ball milled, dried, and loaded into an Ni HIP canister (4 g) and overpacked in an SS HIP canister. The HIP canister system was evacuated and sealed and HIPed (AIP HP1030) at 1320°C at 100 MPa for 2 h. The HIPed sample was then cut into disks of ~16 mm in diameter and ~5–7-mm thick with a ring of Ni metal canister remaining intact on the outside. The sample was characterized (XRD and SEM) with this Ni ring left attached. For SEM analysis, the disk was polished to a 1-μm diamond finish.

2.2 | Sample characterization

XRD analysis was performed on a BRUKER D8 Advance diffractometer using Cu $K\alpha$ radiation (λ = 1.54 Å) and a LYNXEYE detector. The samples were characterized in the range of $10° < 2\theta < 80°$ and with a step size of 0.02° (2θ). Phase identification was undertaken using X'Pert HighScore Plus software. SEM was carried out on samples mounted in epoxy resin and polished to a 1-μm diamond finish and coated with ~10 nm of carbon to avoid charging effects. The SEM was a Tescan Fera 3 instrument with an attached EDS detector (ThermoFisher Scientific) and operated at an accelerating voltage of 15 kV. Pathfinder X-ray microanalysis software was used for EDS data acquisition and standardless EDS data analysis. ImageJ software was used to measure the distance from the canister–wasteform interface to the targeted multiphases in the wasteform, and point analysis of each phase was conducted by EDS. This facilitated elemental profiling of different phases with respect to their distances from the canister–wasteform interface more accurately than for the line scan alone. ImageJ was also used for grayscale-based SEM image analysis to determine the phase abundance.

3 | RESULTS AND DISCUSSION

3.1 | Bulk phase compositions

Though the focus of the paper is the interaction zone, bulk sample analyses from regions near the center of the HIP canister were conducted for both HIP-SS and HIP-Ni. This provided the baseline information such that the phase and compositional changes that occurred at the interaction zone could be clearly characterized and identified. XRD and SEM analyses for materials from the bulk of HIP-SS and HIP-Ni are shown in Figures 1 and 2. Details from the XRD and SEM-EDS analyses are also summarized in Table 2.

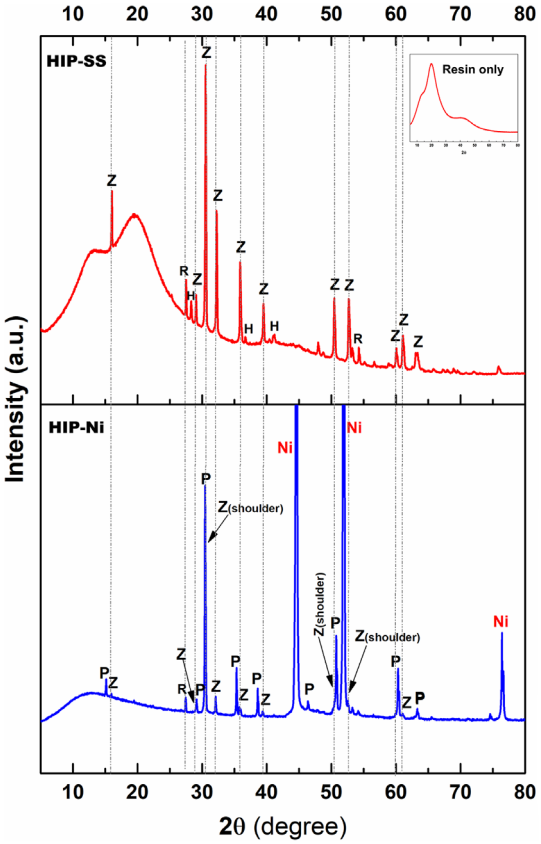

FIGURE 1 XRD patterns of the HIP-SS and HIP-Ni bulk sample showing the main phase zirconolite (Z), hollandite (H), rutile (R), and pyrochlore (P). The broad hump in the pattern for HIP-SS is attributed to the resin mount (resin only XRD is provided for reference), nickel (Ni) peaks in the pattern for HIP-Ni are attributed to the Ni canister left around the outside of the sliced sample. HIP, hot isostatic pressing; SS, stainless steel; XRD, X-ray diffraction

3.1.1 | HIP-SS composition

HIP-SS was a full ceramic composition targeting 80 wt.% zirconolite with 10 wt.% of each of hollandite and rutile. XRD analysis (Figure 1) confirmed the targeted zirconolite (Reference code: 00-054-1132), hollandite (Reference code: 10-078-0012), and rutile (Reference code: 01-076-0318) phase formation. Broad humps in the XRD pattern around 13° and 20° 2θ are attributed to the resin material used for mounting the sample for XRD analysis. XRD identified zirconolite in the 3T polytype. Zirconolite is known to undergo structural transitions with increased lattice substitutions,[21,25] and the zirconolite 3T structure is known to be increasingly stabilized with increased substitutions up to 0.3 f.u. of actinide and when processed under reducing conditions.[22,26]

The sample appeared completely dense in the SEM micrographs (Figure 2) with very little observable porosity. SEM confirmed a uniform microstructure with zirconolite as the predominant phase. The phase abundance was determined to be ~70 vol.% zirconolite with ~19 vol.% hollandite and ~11 vol.% rutile using ImageJ analysis. This analysis was based on area percentage of a two-dimensional slice that was directly converted to vol.%, assuming equiaxed grains. This translates to approximately 71 wt.% zirconolite, 19 wt.% hollandite, and 10 wt.% rutile assuming 4.8, 4.7, and 4.2 g/cm^3 for zirconolite, hollandite, and rutile densities, respectively (noting the large error expected for the density values due to the range of chemistries incorporated in each of the phases). No bright regions indicative of unreacted PuO_2 were observed in the SEM micrographs, confirming complete incorporation of plutonium within the host zirconolite phase. Trace amounts of unreacted Al_2O_3 were also noted (not shown in Figure 2).

The composition for the Pu-bearing zirconolite phase was determined to be $Ca_{0.47}Pu_{0.34}Gd_{0.15}Sm_{0.13}Hf_{0.25}Zr_{0.55}Ti_{1.74}Al_{0.37}O_7$ by SEM-EDS analysis (assuming a total of four cations on the Ca-, Zr-, and Ti sites), which is very close to the target zirconolite composition of $Ca_{0.595}Pu_{0.27}Gd_{0.135}Sm_{0.135}Hf_{0.27}Zr_{0.595}Ti_{1.73}Al_{0.27}O_7$. The elemental analysis also provides evidence for the presence of Pu^{3+} (assuming Ca^{2+}, Gd^{3+}, Sm^{3+}, Hf^{4+}, Zr^{4+}, Ti^{4+}, and Al^{3+}), as per the original design.[18] The hollandite grains were relatively small (~2–4 μm in size) and often associated with similar-sized rutile grains and surrounded by the predominant zirconolite. It was therefore not possible to obtain pure hollandite phase compositions, though several SEM-EDS spot analyses were undertaken. As a result, both zirconolite and rutile materials from the surrounding area were evident in the EDS analysis. To obtain EDS data predominantly related to the hollandite grains, attempts were made to remove contributions from the surrounding zirconolite. This was achieved by assuming all Ca in the hollandite composition due to zirconolite then removing amounts of Ca, Ce, Al, Ti, Zr, Sm, Gd, and Pu according to the experimentally determined zirconolite stoichiometry of $Ca_{0.47}Pu_{0.34}Gd_{0.15}Sm_{0.13}Hf_{0.25}Zr_{0.55}Ti_{1.74}Al_{0.37}O_7$. This suggested a hollandite composition of approximately $Ba_{1.0}(Al_{1.4}Ti^{3+}{}_{0.6})(Ti^{4+})_6O_{16}$, though a slight additional total Ti content (0.8 f.u.) was also noted and likely due to the nearby rutile. All other elements were reduced to values between −0.1 and +0.05 f.u. and therefore assumed negligible. The reduced Al^{3+} content in the hollandite (1.4 f.u. instead of the targeted 2.0 f.u.) is in-line with higher Al content measured in the zirconolite (0.37 f.u. rather than the targeted 0.27 f.u.) and infers that Ti was present in both Ti^{4+} and Ti^{3+} oxidation states with some Ti^{3+} replacing Al^{3+}. The elemental analysis of rutile also showed evidence for zirconolite contamination, again due to its small grain size. The contributions to the EDS data from the surrounding zirconolite were removed similarly to that described for previous hollandite, resulting in

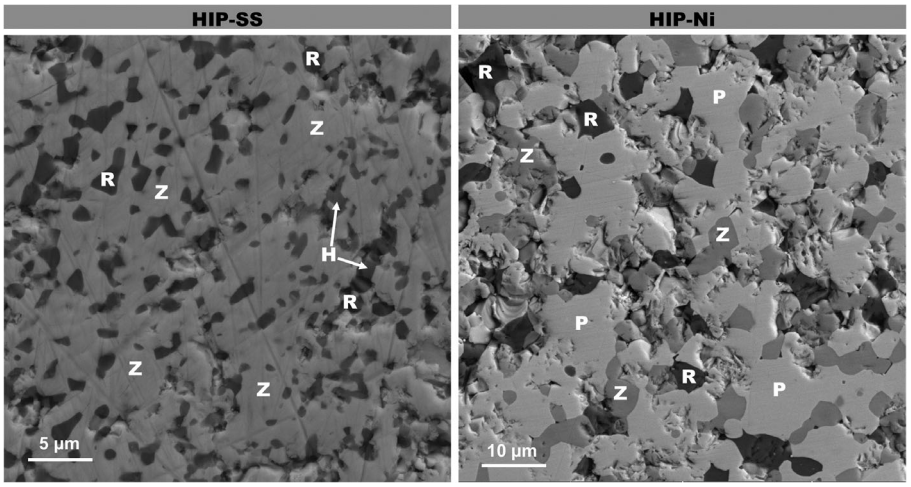

FIGURE 2 Backscattered SEM images of HIP-SS (left) and HIP-Ni (right) from near the center of the HIP canister. Phases are marked accordingly: zirconolite (Z), hollandite (H), pyrochlore (P), and rutile (R). HIP, hot isostatic pressing; SS, stainless steel; SEM, scanning electron microscopy

TABLE 2 Description of areas within the wasteform–SS canister interaction zone[a] and phase composition details

Description		Parameters		
		Distance from interface (μm)[b]	XRD phase analysis*/ composition	SEM-EDS phase composition
Bulk zone	***Bulk canister***	<(−100)	n/a	SS 304
Interaction zone	Modified canister	(−100)–0	n/a	Fe = 67.6, Cr = 19.5, Ni = 9.6, Mn = 2.1, and Si = 1.2 at.% + sparse (Cr,Mn)-rich oxide particles
	Cr-rich oxide	0–20	n/a	Cr_2O_3 with incorporation of oxides of Al (2–5 at.%), Ti (2–8 at.%), Mn (0–8 at.%), Ni (0–5 at.%), and Fe (1–35 at.%)
	Modified wasteform near SS canister	20–60	*Zirconolite TM-rich titanate	$Ca_{0.36}Pu_{0.32}Gd_{0.15}Sm_{0.15}Hf_{0.30}Zr_{0.63}Ti_{1.57}Al_{0.18}Cr_{0.19}Mn_{0.08}Fe_{0.07}O_7$ $\sim(Ca_{0.6}Sm_{0.2}Gd_{0.2}Ba_{0.1})(Pu_{0.7}Zr_{1.0}Hf_{0.4}Al_{1.3}Ti_{12.7}Cr_{3.2}Mn_{0.7}Fe_{0.8})O_{38}$
	Modified wasteform far from SS canister	60–150	*Zirconolite *Hollandite	$Ca_{0.43}Pu_{0.32}Gd_{0.15}Sm_{0.14}Hf_{0.26}Zr_{0.54}Ti_{1.78}Al_{0.26}Cr_{0.02}Mn_{0.03}Fe_{0.05}O_7$ $\sim Ba_{1.0}Al_{0.5}Cr_{0.5}Ti_7O_{16}$
Bulk zone	***Bulk wasteform***	>150	*Zirconolite *Hollandite *Rutile	$Ca_{0.47}Pu_{0.34}Gd_{0.15}Sm_{0.13}Hf_{0.25}Zr_{0.55}Ti_{1.74}Al_{0.37}O_7$ $\sim Ba_{1.0}Al_{1.4}Ti_{6.6}O_{16}$ $\sim Ti_{0.96}Hf_{0.02}Zr_{0.02}O_2$

Abbreviation: SEM-EDS, scanning electron microscopy combined with energy-dispersive X-ray spectroscopy; TM, transition metal; XRD, X-ray diffraction.
[a]The interaction zone or SS–wasteform interface is defined here as the point where metal and oxide materials meet.
[b]Negative values project into the HIP canister, positive values project into the ceramic. *Phases confirmed by XRD analysis.

a rutile composition of $Ti_{0.96}Hf_{0.02}Zr_{0.02}O_2$. Overall, hollandite and rutile were minor phases, and complete plutonium incorporation within the target major zirconolite phase was confirmed by the absence of PuO_2 bright regions.

3.1.2 | HIP-Ni composition

HIP-Ni was designed to form a full-ceramic composition of zirconolite and pyrochlore and with a 30 wt.% actinide waste loading that included 12 wt.% UO_2, 3 wt.% ThO_2, and 15 wt.% PuO_2. XRD (Figure 1) confirmed the targeted zirconolite (Reference code: 00-054-1132), pyrochlore (Reference code: 00-042-0425), and rutile (Reference code: 01-076-0318) phase formation with Ni (Reference code: 01-087-0712) in the pattern attributed to the Ni metal canister left intact around the outside of the sample. Though the peaks attributed to zirconolite in the pattern appear relatively weak compared to the pyrochlore, the alignment with the zirconolite peaks in the pattern for HIP-SS again suggest the 3T polytype. This would infer an actinide (An) content in the zirconolite of f.u. ~0.3. A backscattered SEM micrograph of a sample taken from near the center of the HIP canister (see Figure 2)

again showed the HIPed sample was completely dense. As with HIP-SS, a complete incorporation of plutonium within the ceramic was confirmed as no bright regions indicative of unreacted PuO_2 were observed. The phase assemblage comprised of predominantly pyrochlore, with about 30 vol.% zirconolite and about 10 vol.% rutile, as determined by ImageJ analysis. The SEM-EDS analysis showed the presence of pyrochlore with composition $(Ca_{0.84}Gd_{0.16}Zr_{0.25}U_{0.38}Th_{0.06}Pu_{0.37}Ti_{1.88}Al_{0.03}Ni_{0.03})O_7$ (assuming a total of four cations on the available cation sites) and incorporating trace amounts of Al and Ni. The zirconolite composition was determined to be $Ca_{0.72}Gd_{0.13}Pu_{0.22}U_{0.09}Th_{0.02}Zr_{0.87}Ti_{1.76}Al_{0.12}Ni_{0.06}O_7$ and rutile was $Ti_{0.95}Zr_{0.05}O_2$. The elemental analysis suggests that at least part of the U and/or Pu is present in higher oxidation state than U^{4+} and Pu^{3+} (again assuming Ca^{2+}, Gd^{3+}, Th^{4+}, Zr^{4+}, Ti^{4+}, Al^{3+}, and Ni^{2+}). It is noted that experimental evidence for U^{4+},[27] as well as for mixed $U^{4+/5+}$ have been measured during the HIP consolidation of U-bearing zirconolites and pyrochlore,[13,25] the valence state being influenced by several aspects such as crystal chemistry, charge compensation mechanisms, and consolidation conditions. It was observed that the majority of the actinides were incorporated within the pyrochlore structure (An = 0.81 f.u.) with relatively less amounts of actinides within the less abundant zirconolite phase (An = 0.33 f.u.). The amount of actinide materials measured within the zirconolite is in alignment with the formation of the 3T polytype and thus in agreement with the XRD data. Ni was present at low to trace levels within the pyrochlore and zirconolite phases, respectively, and is believed to be due to the migration of Ni from the canister wall, particularly for this relatively small HIP canister (internal volume = 2.5 ml, inner diameter = 11 mm).

The predominant aim of the current work was to compare the effects of canister material (SS or Ni) on the wasteform –HIP canister interaction for two zirconolite-rich full ceramics, for the first time. Although the bulk wasteforms produced are both Pu-bearing zirconolite-rich ceramics, the study is limited by the fact that the wasteform designs are different and therefore contain differing secondary phases. The influences of the secondary phases on the interaction zone as well as of the canister material on the secondary phases are therefore not directly comparable; however, it is still possible to make a number of important observations.

3.2 | SS HIP canister–wasteform interaction

Microstructural analysis of the HIP canister and wasteform material near to the SS canister–wasteform interface was undertaken after HIPing using SEM, and Figure 3 shows a digitally stitched image of a series of SEM images to show the interaction zone, including canister and wasteform. The interaction zone overall can be divided into three distinct areas that are as follows: (1) modified canister, (2) chromium-rich oxide layers, and the (3) modified wasteform. The modified wasteform area can itself be further divided into two areas being (i) modified wasteform near SS canister and (ii) modified wasteform far from SS canister. The distance from the canister–wasteform interface for each of these areas is provided in Table 2 and Figure 3.

3.2.1 | Bulk canister

The pre-HIPed SS 304 canister wall thickness was measured to be ~2.9 mm. Several HIP canister wall thickness measurements were taken during SEM analysis of the post-HIPed sample, and no wall thinning was observed. Instead, in some areas, the canister wall thickness was observed to increase (~20%) due to the compressive strain experienced during the HIP cycle. The amount of thickening was, however, quite variable and dependent on the extent of buckling of the canister wall during HIPing. Elemental analysis (at.%) using EDS analysis returned a bulk SS composition of Fe = 67.6, Cr = 19.5, Ni = 9.6, Mn = 2.1, and Si = 1.2.

3.2.2 | Modified canister

Sparse, micron sized Cr- and Mn-rich oxide particles (Cr:Mn ~ 2:1) were observed to be distributed within the modified SS region as shown in Figure 3. The very odd Fe/Si oxide particle was also noted in this region. Some of these particles appeared to be smeared and/or ejected from the bulk leaving a cavity (~1–2 μm), though this is likely to be a result of metallographic sample preparation (grinding and polishing).

SEM-EDS was undertaken at various positions throughout the SS HIPed canister. Results from the elemental profiling from the bulk of the unmodified SS canister toward the interface with the wasteform oxide layer are shown in Figure 4. Cr depletion from ~17.8 to 6.5 at.% was clearly observed in the 100-μm area adjacent to the interface with the wasteform. Similarly, Mn was reduced from ~2.0 to 0 at.% in the same area. As a result of the migration of Cr and Mn from the HIP canister, relative increases in the at.% of both Fe and Ni were noted (see, e.g., Ni at.% in Figure 4). The results indicate that compositional changes to the SS HIP canister are confined to the 100-μm region (highlighted in Figure 4) immediately adjacent to the canister–wasteform interface. In addition, there was no

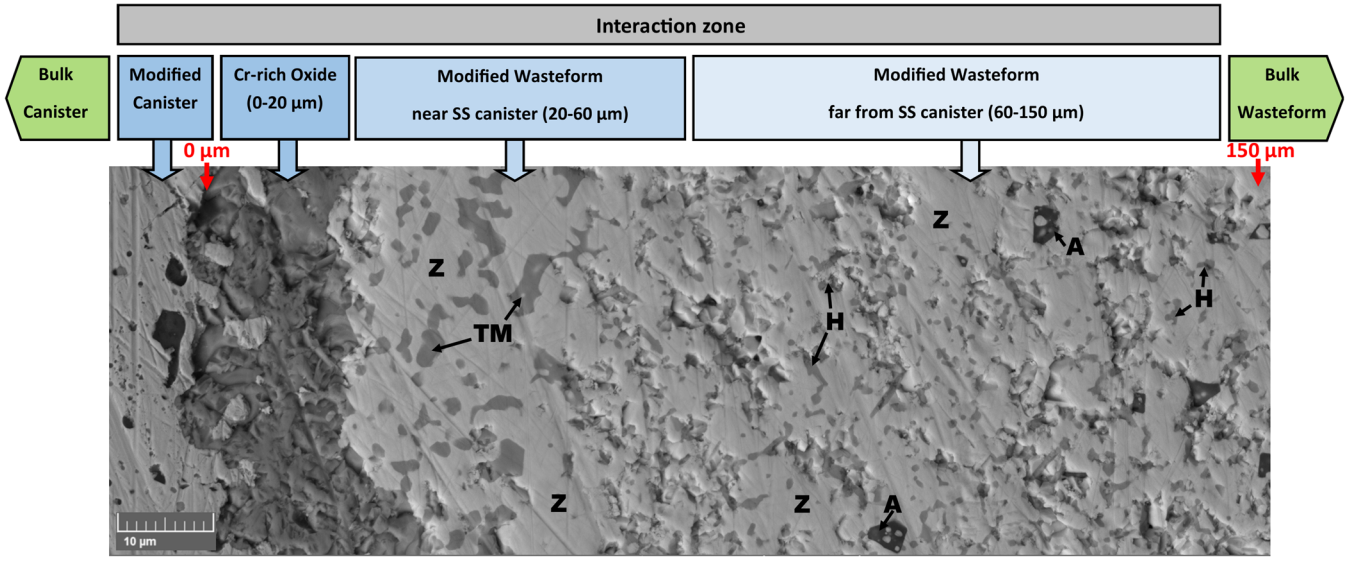

FIGURE 3 Backscattered SEM image (digitally stitched) of the SS canister–wasteform interface region. Phases are marked accordingly: zirconolite (Z), transition metal (TM)-rich titanate, hollandite (H), and alumina (A). SEM, scanning electron microscopy; SS, stainless steel; TM, transition metal

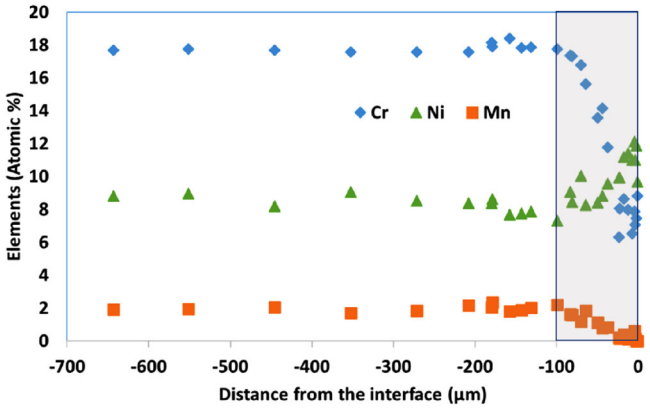

FIGURE 4 Elemental profiling of the SS canister material from the bulk of the unmodified SS HIP canister to the interface with the wasteform. The shaded region ((−100)–0 μm) represents the modified canister. HIP, hot isostatic pressing; SS, stainless steel

gap observed between the modified SS canister region and the wasteform at the interface, as has been reported previously for some HIPed wasteforms.[28]

3.2.3 | Chromium-rich oxide

A Cr-rich oxide layer of ~10–20 μm (Figure 3) formed immediately adjacent to the HIP canister, as has been described previously.[16,24] Several EDS spot analyses were undertaken of this Cr-rich oxide layer, and these showed varying contents of Al (2–5 at.%), Ti (2–8 at.%), Mn (0–8 at.%), Ni (0–5 at.%), and Fe (1–35 at.%). The oxide layer is attributed to the diffusion of Mn, Ni, Fe, and particularly Cr out of modified SS canister and subsequent reaction and oxidation by the HIPed material.[16] Some cavities (<10 vol.%) were observed within this Cr-rich oxide layer; however, due to the nature of the sample, it was not possible to conclude whether these were voids in the sample or polishing defects.

3.2.4 | Modified wasteform near SS canister

The modified wasteform near SS canister manifested as a 40-μm region immediately adjacent to the Cr-rich oxide layer. The wasteform phase assemblage in this region was modified relative to the bulk composition. Though zirconolite remained the predominant phase, its composition was altered in order to incorporate quantities of Cr and other canister chemistry. The average zirconolite composition immediately adjacent (<10 μm from the Cr-rich oxide layer) was determined via EDS analysis to be $Ca_{0.36}Pu_{0.32}Gd_{0.15}Sm_{0.15}Hf_{0.30}Zr_{0.63}Ti_{1.57}Al_{0.18}Cr_{0.19}Mn_{0.08}Fe_{0.07}O_7$ (again assuming a total of four cations on the Ca-, Zr-, and Ti sites). The composition includes Cr, Fe, and Mn (a total of 0.34 f.u. of migrated canister material) with a subsequent reduction of Ti and Al (a total of 0.36 f.u. less Ti and Al), relative to the bulk material composition. This follows given the ionic radii of Cr^{3+}, Fe^{3+}, and Mn^{4+} in sixfold coordination are 0.0615, 0.0645, and 0.053 nm, respectively, and Ti^{4+} is 0.0605 nm.[29] Though the oxidation states of Cr, Fe, and Mn at the canister edge were not determined in this study, the previous work[30] has demonstrated that a single-dominant Cr environment (Cr^{3+} with near-edge features consistent with occupation

of octahedral sites) is present within zirconolite. If Mn was to exist in Mn^{2+} oxidation state, then alternate incorporation mechanisms, for example, Mn^{2+} (0.096 nm in eight-coordination) incorporation on the Ca site (0.112 nm in eight-coordination) could be envisaged.[29] In addition, there is a subtle increase in the Zr and Hf content (a total of 0.13 f.u.) and decrease in Ca content (0.11 f.u.), relative to the bulk material. This change may provide charge balance for the system to facilitate the incorporation of transition metals (TMs) with oxidation states <3+ on the Ti^{4+} site. Notably, there is little change to the Pu content of the zirconolite.

In addition to the change in zirconolite composition, the modified wasteform near SS canister was characterized by the apparent absence of the relatively small grained (~2–4 μm) rutile and hollandite, and instead a single secondary phase of ~5–10 μm in size was observed. Several EDS spot analyses were undertaken, and these indicated a TM-rich titanate of a different composition to that measured for the hollandite in the bulk canister. The composition of the titanate was determined to be $(Ca_{0.6}Sm_{0.2}Gd_{0.2}Ba_{0.1})(Pu_{0.7}Zr_{1.0}Hf_{0.4}Al_{1.3}Ti_{12.7}Cr_{3.2}Mn_{0.7}Fe_{0.8})O_{38}$, which is close to the stoichiometry for loveringite (a typical theoretical formula of $(Ca,Ce)(Ti,Fe,Cr,Mg)_{21}O_{38}$)),[31] though it was possible that spot analyses also included trace amounts of the adjacent zirconolite. Based on the analysis of the TM-rich titanate phase listed in Table 2, we have investigated the possibility that this phase is loveringite, a complex oxide of the crichtonite group that typically forms in titanate-rich systems when a particular mix of TMs and medium-to-large trivalent and divalent metal cations are available. In the previous work on Synroc C, for example, loveringite is found as a minor phase in formulations with Fe_2O_3 included in the bulk composition.[13] It is also well known from natural systems that crichtonite group minerals may incorporate lanthanides and actinides. Gatehouse et al.[32] provided a detailed description of the structure of loveringite, and Wülser et al.[33] gave an excellent summary of the structure and composition of this mineral group, in particular, the cation composition of the various crystallographic sites. In brief, crichtonite is a rhombohedral layered structure that conforms to a complex formula written as $^{XII}A^{VI}B^{VI}C_{18}{}^{IV}T_2O_{38}$, wherein the Roman numerals give the coordination numbers of the cation sites. Based on the information on site occupancies in the crichtonite group given by Wülser et al. [33], we have attempted to fit the composition of the "TM-rich titanate phase" given in Table 2 to the structural/general formula of crichtonite. The results of this exercise are given in Table 3 where we see good agreement with the cation site distribution of loveringite based on previous analyses and structure refinements of natural samples. Loveringite has previously been reported as a secondary phase in certain Synroc formulations and is considered a durable titanate host phase for the accommodation of some components of high-level wastes [13,34]. However, given the significant quantity of plutonium in this phase (~9 wt.%), it is necessary to have a detailed understanding of the Pu speciation, dissolution behavior, and Pu release rates from loveringite in order to model the long-term behavior for this HIPed zirconolite-rich Pu-bearing wasteform in a geological repository. Given the apparent presence of Ti^{3+} in the interaction zone, it may be postulated that Pu is present in the 3+ valence state. Further, crystallographic sites are available in loveringite with potential to accept both Pu^{3+} or the smaller ionic radius Pu^{4+}. Although beyond the scope of the current work, these aspects of Pu speciation and loveringite's aqueous durability as well as confirmation of this mineral phase allocation is required, and this is the subject of future work.

The TiO_2 buffer phase performs as designed and deals with the changes in chemistry at the interaction zone by facilitating titanate phase formation. Interestingly, TiO_2 is completely consumed in the modified wasteform near SS canister zone as a result of reorganization of the phase assemblage and the formation of loveringite.

The destabilization and therefore the absence of hollandite within the interaction zone (modified wasteform near SS canister) may mean that Cs is without a host phase if it were to be present in this region. This may impact its release during aqueous dissolution studies; however, this aspect requires further investigation, including an understanding of any interaction of Cs with the HIP canister material.

3.2.5 | Modified wasteform far from SS canister

In the next ~90 μm (60–150 μm from the canister–wasteform interface), the phase constitution returned similarly to that of the bulk material, with zirconolite the predominant phase and minor hollandite apparent. Subtle differences in the elemental composition for each of the phases were noted compared to the bulk and these are summarized in Table 2. Again, in order to obtain EDS data predominantly related to the small hollandite grains (2–4 μm), contributions from the surrounding zirconolite were removed similarly to that described previously. This returned a hollandite composition containing Cr with approximate formula $Ba_{1.0}(Al_{0.5}Cr_{0.5}Ti^{3+})(Ti^{4+})_6O_{16}$ at 75 μm from the canister–wasteform interface. In addition to the incorporation of Cr content in the hollandite in this region, the composition also suggested a higher Ti^{3+} content relative to the bulk material, and this is consistent with the reducing influence of the nearby HIP canister.

TABLE 3 Assignment of cations to the crystallographic sites of loveringite (from Table 2)

Site	CN[a]	Occ.[b]	Ca, Ba	Ln	Pu	Zr, Hf	Al	Ti	Cr	Mn	Fe	Sum
			0.7	0.4	0.7	1.4	1.3	12.7	3.2	0.7	0.8	21.9
M0	12	1	0.7	0.4	–	–	–	–	–	–	–	1.1
M1	6	1	–	–	0.7	0.3	–	–	–	–	–	1
M2	4	2	–	–	–	1.1	–	–	–	0.7	–	1.8
M3	6	6	–	–	–	–	1.3	0.7	3.2	–	0.8	6
M4	6	6	–	–	–	–	–	6	–	–	–	6
M5	6	6	–	–	–	–	–	6	–	–	–	6

[a]CN = coordination number.
[b]Occ. = occupancy, provided as a guide only. Definitive allocation of the cations to the crystallographic sites requires further experimentation and confirmation.

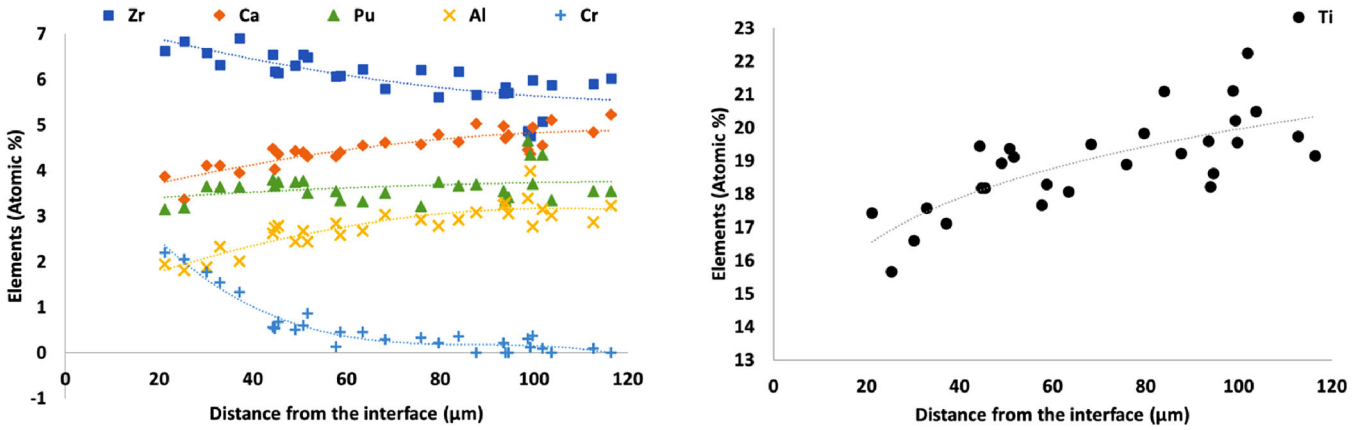

FIGURE 5 Elemental profiling for the zirconolite phase from the canister–wasteform interface toward the bulk wasteform (dashed lines are provided as indication)

A detailed profiling of the elemental composition of zirconolite, as a function of distance from the canister–wasteform interface and throughout the modified wasteform near SS canister and far away from SS canister, is provided in Figure 5. Importantly, no change to the plutonium content in the zirconolite was observed, irrespective of proximity to the canister–wasteform interface. The amount of Cr, Fe, Mn, and Ni diffused from the HIP canister and incorporated in the zirconolite gradually decreased as EDS measurements were taken further from the interface, until ~120–150 μm where the levels were below the detection limit. This is clearly demonstrated by the profile for Cr (see Figure 5). The Ti and Al contents were evidently linked to the incorporation of canister material, simultaneously, increased with distance from the canister–wasteform interface. This was unsurprising given they share the same site within the zirconolite structure. Subtle, and opposing changes to the Zr and Ca content were also observed throughout the modified wasteform - near SS canister and far away from SS canister area, with Zr gradually decreasing and Ca gradually increasing with distance from the interface. All elements had returned to values close to the bulk composition for zirconolite between ~120 and 150 μm from the interface.

The Cr- and Ba contents of the TM-rich titanate and hollandite phases were also profiled, and the results are provided in Figure 6. Independent of whether the Cr is incorporated within the TM-rich titanate or hollandite phase, its content gradually decreased as measurements were undertaken further from the canister–wasteform interface, until they were below the detection limit at around 120–150 μm. The Ba content showed two distinct regions, the modified wasteform near SS canister shows low Ba in concurrence with the formation of the TM-rich titanate, whereas the modified wasteform far away from SS canister shows relatively higher Ba consistent with its incorporation in hollandite. The Ba content in the hollandite appears relatively variable from EDS analysis from ~60–150 μm (see Figure 6). This is likely due to the small nature of the hollandite grain structure (2–4 μm) and potential for the inclusion of nearby zirconolite in the EDS analyses.

It was evident that Cr was the main element migrating from the HIP canister and toward the bulk ceramic material, both in zirconolite or other TM-rich titanate

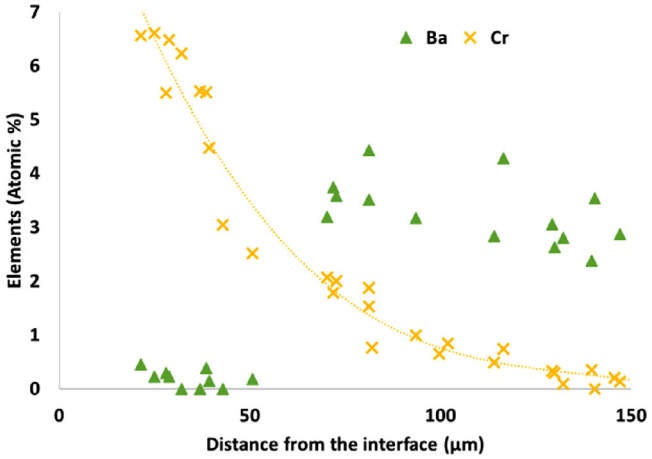

FIGURE 6 Elemental profiling for Cr and Ba in the TM-rich titanate and hollandite phases from the canister–wasteform interface toward the bulk wasteform (the dashed line is provided as indication). The TM-rich titanate is evident from ~20 to 50 μm from the interface with hollandite evident at regions >~50 μm from the interface and with the Cr content decreasing in both phases with increasing distances from the interface. TM, transition metal

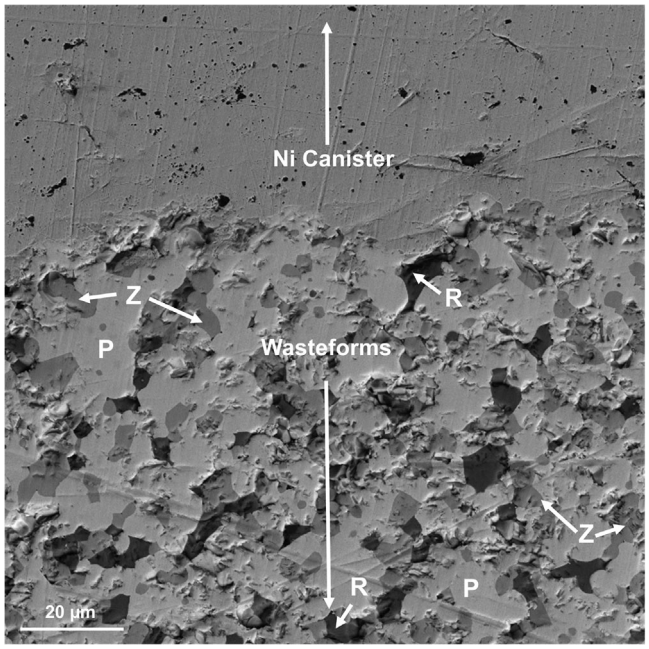

FIGURE 7 Backscattered SEM image of the Ni-metal canister–wasteform interface showing the sharp boundary between the Ni canister and the wasteform. The light gray phase in the wasteform is pyrochlore (P), the mid gray phase is zirconolite (Z), and the dark phase is rutile (R). The dark particles in the Ni canister are Ni silicide. SEM, scanning electron microscopy

or hollandite phases. From a compositional perspective, larger amounts of Cr were incorporated within the TM-rich titanate material, with relatively less amounts incorporated within hollandite and zirconolite. There was no evidence for the migration of Cr, Fe, Mn, and Ni from the HIP canister beyond the ~150-μm distance from the HIP canister–wasteform interface.

As evident from Figures 4–6, we collected a large number of EDS data points from different grains of different phases. However, all these grains existed at marginally different distances from the interface, as can be seen in Figure 3. To be able to include error(s) to these data points, we need to find multiple grains of the same phase at exactly the same distance from the interface, which was practically not feasible in the present case. The variation in the values of multiple data points (data points are highly consistent) within a few microns range is an indirect representation of the error(s) in these data sets.

3.3 | Ni HIP canister–wasteform interaction

Similarly, to that discussed for HIP-SS, microstructural analyses of the HIP canister and wasteform material near to the Ni canister–wasteform interface were undertaken after HIPing of HIP-Ni using SEM-EDS analyses. Figure 7 shows a high magnification SEM image of this interaction zone. Due to the general lack of interaction between the Ni canister and the ceramic material, the interaction zone of HIP-Ni could not be divided into distinct areas similarly to that for HIP-SS. Instead, the following discussion will provide general descriptions for the Ni-canister and wasteform at the interface, with comparisons made to that of the corresponding bulk materials.

3.3.1 | HIP canister

HIP-Ni was HIPed in Nickel 200 alloy canister with a pre-HIPed wall thickness of ~3.1 mm. As the Ni canister was HIPed with an SS overpack, the outer edge of the Ni canister wall was obscured during sample preparation for SEM characterization and this prevented the exact measurement of the post-HIP Ni-metal wall thickness; however, an intact canister maximum wall thickness measurement of ~3.1 mm was observed. Therefore, it was concluded that no canister wall thinning occurred during HIPing. It may be possible that the Ni canister wall thickened during HIPing, similarly to that noted for the HIP-SS sample; however, this could not be confirmed.

In contrast to HIP-SS, no oxide particles or associated cavities were observed within the Ni canister in the region near the interface. However, some Ni silicide intermetallic compounds were identified using SEM-EDS characterization (see Figure 7). Figure S1 provides elemental profiling data of the canister material at the canister–wasteform

TABLE 4 Description of areas within the wasteform–Ni canister interaction zone[a] and phase composition details

Description		Parameters		
		Distance from interface (μm)[b]	XRD phase analysis*/ composition	SEM-EDS phase composition
Bulk zone	***Bulk canister***	<(−100)	*Ni	Ni, small amount of nickel silicide
Interaction zone	Canister	(−100)–0	*Ni	Ni, small amount of nickel silicide
	Wasteform	0–10	*Pyrochlore *Zirconolite *Rutile	$(Ca_{0.81}Gd_{0.15}Zr_{0.24}U_{0.38}Th_{0.06}Pu_{0.36})(Ti_{1.88}Al_{0.03}Ni_{0.09})O_7$ $(Ca_{0.69}Gd_{0.10}Pu_{0.22})(Zr_{0.85}U_{0.09}Th_{0.03})Ti_{1.77}Al_{0.12}Ni_{0.13}O_7$ $Ti_{0.93}Zr_{0.05}Al_{0.01}Ni_{0.01}O_2$
Bulk zone	***Bulk wasteform***	>10	*Pyrochlore *Zirconolite *Rutile	$(Ca_{0.84}Gd_{0.16}Zr_{0.25}U_{0.38}Th_{0.06}Pu_{0.37})(Ti_{1.88}Al_{0.03}Ni_{0.03})O_7$ $(Ca_{0.72}Gd_{0.13}Pu_{0.22})(Zr_{0.87}U_{0.09}Th_{0.02})Ti_{1.76}Al_{0.12}Ni_{0.06}O_7$ $Ti_{0.95}Zr_{0.05}O_2$

Abbreviation: SEM-EDS, scanning electron microscopy combined with energy-dispersive X-ray spectroscopy; XRD, X-ray diffraction.

[a]The interaction zone or Ni–wasteform interface is defined here as the point where metal and oxide materials meet.

[b]Negative values project into the HIP canister, positive values project into the ceramic. *Phases confirmed by XRD analysis.

interface. In addition, no gap was observed between the Ni-canister and the wasteform, and no porosity or NiO was detected at the interface. Instead, a sharp boundary was observed between the Ni and the titanate wasteform, indicating the absence of any notable chemical reaction.

3.3.2 | Wasteform at the interaction zone

SEM-EDS analysis of the various phases present in the region immediately adjacent to the Ni canister indicated predominantly pyrochlore (light gray phase) with smaller amounts of zirconolite (mid gray phase) and rutile (dark phase), as shown in Figure 7. There were no obvious changes to the phase abundance compared to that of the bulk material. In the area immediately adjacent to the Ni canister (<10 μm), both pyrochlore and zirconolite showed minor increases in the amount of Ni incorporated within their structures, as summarized in Table 4. In general terms, the measured compositions gradually returned to those observed for the bulk pyrochlore and zirconolite at distances approximately >20 and 50 μm from the interaction zone, respectively. The incorporation rate of Ni within both the pyrochlore and zirconolite phases was relatively low and close to the limit of detection, resulting in some irregular measurements; however, elemental profiling for zirconolite and pyrochlore as a function of distance from the HIP canister–wasteform interface was undertaken and is provided in Figure S1.

In Table 4, the zirconolite and pyrochlore compositions are expressed with Ni^{2+} (ionic radius 0.069 nm in sixfold coordination) on the Ti^{4+} site (ionic radius 0.061 nm in sixfold coordination). This seems reasonable given the Ti site in zirconolite can accommodate cations with radii ranging from 0.0535 to 0.083 nm and the B site in pyrochlore can similarly accommodate cations with radii ranging from 0.060 to 0.083 nm.[35] Further, an extensive solubility of Mg^{2+}, Al^{3+}, Ti^{3+}, Fe^{3+}, and Nb^{5+} species within the Ti^{4+} site of zirconolite has also been demonstrated [20].

3.4 | Overall impact of canister–wasteform interaction

The HIP-Ni sample with its Ni HIP canister showed almost no interaction zone with only minor diffusion of Ni from the canister toward the wasteform, and the diffused Ni successfully incorporated into durable zirconolite and pyrochlore titanate ceramic phases. The HIP-SS sample with the SS HIP canister showed ~100–120 μm of interaction zone dominated by Cr diffusion from the canister material into the wasteform. This Cr was incorporated into durable zirconolite, hollandite, and loveringite titanate ceramics. Interestingly, when comparing these samples, the minor Ni diffusion determined for HIP-Ni was observed to progress to center of the canister; however Cr diffusion was restricted to ~120 μm from the interaction zone in the HIP-SS sample. The apparent enhanced mobility of Ni relative to Cr may be attributed to the absence of any oxide layer formation at the interface, which potentially could act as a barrier for further canister material migration. By contrast, the HIP-SS sample was noted to have a 10–20-μm Cr-oxide layer that has likely restricted a further progression of Cr, Fe, and Ni into the ceramic material. Also, the smaller diameter of the HIP-Ni canister (internal volume = 2.5 ml, inner diameter = 11 mm) relative to the HIP-SS canister provides a shorter distance for Ni to migrate throughout the wasteform. Ni has a relatively weak affinity for oxygen compared with that for Cr. The free energy of formation, per gram atom of oxygen at 25°C

(kcal), for Cr_2O_3 is −84.5 and for NiO is −51.6.[36,37] Because of this oxygen affinity difference, the possibility of an oxide layer formation for the Ni canister is much lower than that for Cr in the SS canisters.

Notably, in the interaction zone for both samples, the major zirconolite (and pyrochlore) phase remained intact, and though hollandite was replaced with a TM-rich loveringite type titanate in HIP-SS, this phase is also considered a durable and acceptable wasteform phase. The overall wasteform phase assemblage for HIP-Ni (pyrochlore, zirconolite, and rutile) was not impacted due to the very minor Ni migration.

It is also important to note that the magnitude of this interaction zone was not significant in terms of the total ceramic wasteform. With regards to the SS HIP canisters (internal volume = 17 ml, inner diameter = 32 mm, 20-g sample size) investigated in the current work, the interaction zone corresponds to ∼2–5 vol.% of the wasteform material. However, when considering an industrial scale HIPed wasteform (e.g., 6 L and ∼20 kg) and assuming the same interaction mechanisms and zone thicknesses, the modified zone would translate to only ∼0.2–0.3 vol.%. Therefore, the relatively small extent of the interaction zone and the fact that the HIP canister–wasteform interaction did not produce any obviously less durable phases make both Ni and SS HIP canisters viable options for zirconolite-rich titanate wasteforms for plutonium.

4 | CONCLUSIONS

Pu-bearing zirconolite-rich full ceramic wasteforms samples, HIPed in SS and Ni canisters, were successfully characterized using SEM-EDS and XRD, with a focus on changes to the HIP canister wall thickness and composition in the interaction zone at the canister–wasteform interface. The phase chemistries at the center of the canister were also compared with that in the interaction zone. First, no HIP canister wall thinning was observed as a result of HIPing. HIPing caused high temperature elemental diffusion across the canister-wasteform interface, and these diffused elements were incorporated within durable titanate ceramic phases. Both zirconolite and pyrochlore demonstrated flexibility in their ability to incorporate a range of cations, including Cr, Fe, and Ni uptake into their structures with no free actinide oxide observed either in the bulk or at the canister–wasteform interface. The interaction layer, though smaller, results in no deleterious phases that would impact wasteform performance or the HIP canister properties. The current work has shown that the interaction zone was relatively minor, both in terms of length (∼100–120 μm) and volume (∼0.2%–0.3% for an estimated 6 L/20 kg HIPed wasteform in a SS canister). Both Ni HIP canister and SS HIP canister are suitable for use with zirconolite-based ceramic Pu-bearing wasteforms at the industrial scale. Future work will target a common wasteform design to allow a more direct comparison of the impact of the HIP canister material on the interaction zone and delineate any influence of wasteform compositional variations.

ACKNOWLEDGMENTS

We would like to thank Miodrag Jovanovic for his assistance in Pu-bearing sample preparation, Neil Webb for providing HIP support, and Jialuo (Carol) Ke for phase abundance analyses. This work was partly funded by Nuclear Decommissioning Authority, United Kingdom. Open access publishing facilitated by Australian Nuclear Science and Technology Organisation, as part of the Wiley - Australian Nuclear Science and Technology Organisation agreement via the Council of Australian University Librarians.

ORCID

Pranesh Dayal https://orcid.org/0000-0002-7324-5258
Rifat Farzana https://orcid.org/0000-0001-8611-8744
Yingjie Zhang https://orcid.org/0000-0001-6321-4696
Gregory R. Lumpkin https://orcid.org/0000-0002-9266-0457

REFERENCES

1. World Nuclear Association "Plutonium". https://www.world-nuclear.org/information-library/nuclear-fuel-cycle/fuel-recycling/plutonium.aspx
2. Deissmann G, Neumeier S, Modolo G, Bosbach D. Review of the durability of potential plutonium wasteforms under conditions relevant to geological disposal. FZ Julich/Brenk Systemplanung Report to NDA RWMD; 2011.
3. Ojovan MI, Lee WE, Kalmykov SN. An introduction to nuclear waste immobilisation. ISBN: 9780081027035. Elsevier; 2019.
4. Gregg DJ, Farzana R, Dayal P, Holmes R, Triani G. Synroc technology: perspectives and current status. J Am Ceram Soc. 2020;103(10):5424–41.
5. Lutze W, Ewing RC. Radioactive waste forms for the future. 1988, p. 233–334.Elsevier Science Publishers, Amsterdam, ISBN: 0-444-87104-7
6. Ringwood A, Kesson S, Ware N, Hibberson W, Major A. Immobilisation of high level nuclear reactor wastes in SYNROC. Nature. 1979;278(5701):219–23.
7. Zhang Y, Stewart M, Li H, Carter M, Vance E, Moricca S. Zirconolite-rich titanate ceramics for immobilisation of actinides—waste form/HIP can interactions and chemical durability. J Nucl Mater. 2009;395(1–3):69–74.
8. Gregg DJ, Vance ER. Synroc tailored waste forms for actinide immobilization. Radiochim Acta. 2017;105(11):907–25.
9. Holmes R, Abboud A, Bigrigg B, Gregg DJ, Deura M, Townsend W, et al. Current status of the Synroc waste treatment facility, waste management 20(WM'20), paper 20263, Phoenix, AZ, USA, March 8–12, 2020.

10. Thunholm R, Shipley J, Holmes R, Gregg DJ, Bigrigg B, Fleming P, et al. Technology maturation of hot isostatic pressing for nuclear waste treatment, waste management 20 (WM'20), paper 20259, Phoenix, AZ, USA, March 8–12, 2020.
11. Maddrell E. Hot isostatically pressed wasteforms for future nuclear fuel cycles. Chem Eng Res Des. 2013;91(4):735–41.
12. Carter M, Li H, Zhang Y, Vance E, Mitchell D. Titanate ceramics for immobilisation of uranium-rich radioactive wastes arising from ^{99}Mo production. J Nucl Mater. 2009;384(3):322–6.
13. Farzana R, Zhang Y, Dayal P, Aly Z, Holmes R, Triani G, et al. Pyrochlore glass-ceramics for the immobilization of molybdenum-99 production wastes: Demonstrating scalability and flexibility to waste stream variance. J Eur Ceram Soc. 2021;41(14):7269–81.
14. Vance ER, Grant C, Karatchevtseva I, Aly Z, Stopic A, Harrison J, et al. Immobilization of iodine via copper iodide. J Nucl Mater. 2018;505:143–8.
15. Gregg DJ, Vance ER, Dayal P, Farzana R, Aly Z, Holmes R, et al. Hot Isostatically Pressed (HIPed) fluorite glass-ceramic wasteforms for fluoride molten salt wastes. J Am Ceram Soc. 2020;103(10):5454–69.
16. Li H, Zhang Y, McGlinn P, Moricca S, Begg B, Vance E. Characterisation of stainless steel–Synroc interactions under hot isostatic pressing (HIPing) conditions. J Nucl Mater. 2006;355(1–3):136–41.
17. Zhang Y, Li H, Moricca S. Pyrochlore-structured titanate ceramics for immobilisation of actinides: hot isostatic pressing (HIPing) and stainless steel/waste form interactions. J Nucl Mater. 2008;377(3):470–5.
18. Vance E, Jostsons A, Moricca S, Stewart M. Synroc derivatives for excess weapons plutonium. Ceram Trans. 1998;93:323–9.
19. Macfarlane A. Immobilization of excess alternative to glass. Sci Global Secur. 1998;7(3):271–309.
20. Blackburn LR, Bailey DJ, Sun S-K, Gardner LJ, Stennett MC, Corkhill CL, et al. Review of zirconolite crystal chemistry and aqueous durability. Adv Appl Ceram. 2021;120(2):69–83.
21. Coelho A, Cheary R, Smith K. Analysis and structural determination of Nd-substituted zirconolite-4M. J Solid State Chem. 1997;129(2):346–59.
22. Begg B, Day R, Brownscombe A. Structural effect of Pu substitutions on the Zr-site in zirconolite. MRS Online Proc Libr (OPL). 2000;663. https://doi.org/10.1557/PROC-663-259
23. Guo X, Gin S, Lei P, Yao T, Liu H, Schreiber DK, et al., Self-accelerated corrosion of nuclear waste forms at material interfaces. Nat Mater. 2020;19(3):310–6.
24. Blackburn LR, Cole MR, Gardner LJ, Bailey DJ, Kuman M, Mason AR, et al. Synthesis and characterisation of HIP $Ca_{0.80}Ce_{0.20}ZrTi_{1.60}Cr_{0.40}O_7$ zirconolite and observations of the ceramic–canister interface. MRS Adv. 2021;6(4):112–8.
25. Vance ER, Lumpkin GR, Carter ML, Cassidy DJ, Ball CJ, Day RA, et al., Incorporation of uranium in zirconolite ($CaZrTi_2O_7$). J Am Ceram Soc. 2002;85(7):1853–9.
26. Gilbert M, Selfslag C, Walter M, Stennett M, Somers J, Hyatt N, et al. Synthesis and characterisation of Pu-doped zirconolites–$(Ca_{1-x}Pu_x)Zr(Ti_{2-2x}Fe_{2x})O_7$. IOP Conference Series: Materials Science and Engineering, SanFrancisco, USA. IOP Publishing; 2010. p. 012007.
27. Blackburn LR, Crawford R, Walling SA, Gardner LJ, Cole MR, Sun S-K, et al. Influence of accessory phases and surrogate type on accelerated leaching of zirconolite wasteforms. NPJ Mater Degrad. 2021;5(1):1–11.
28. Zhang Y, Li H, McGlinn PJ, Yang B, Begg B. Stainless steel/glass–ceramic interactions under hot isostatic pressing (HIPing) conditions. J Nucl Mater. 2008;375(3):315–22.
29. ASTM C1285. Standard test methods for determining chemical durability of nuclear, hazardous, and mixed waste glasses and multiphase glass ceramics: the product consistency test (PCT); 2014.
30. Blackburn LR, Sun S-K, Lawson SM, Gardner LJ, Ding H, Corkhill CL, et al. Synthesis and characterisation of $Ca_{1-x}Ce_xZrTi_{2-2x}Cr_{2x}O_7$: Analogue zirconolite wasteform for the immobilisation of stockpiled UK plutonium. J Eur Ceram Soc. 2020;40(15):5909–19.
31. Cabella R, Gazzotti M, Lucchetti G. Loveringite and baddeleyite in layers of chromian spinel from the Bracco ophiolitic unit, Northern Apennines, Italy. Can Mineral. 1997;35(4):899–908.
32. Gatehouse BM, Grey I, Campbell I, Kelly P. The crystal structure of loveringite, a new member of the crichtonite group. Am Mineral. 1978;63(1–2):28–36.
33. Wülser P-A, Meisser N, Brugger J, Schenk K, Ansermet S, Bonin M, Bussy F. Cleusonite,(Pb, Sr) (U^{4+}, U^{6+}) (Fe^{2+}, Zn)$_2$(Ti, Fe^{2+}, Fe^{3+})$_{18}$(O, OH)$_{38}$, a new mineral species of the crichtonite group from the western Swiss Alps. Eur J Mineral. 2005;17(6):933–42.
34. Stefanovskii S, Yudintsev S, Nikonov B, Stefanovskaya O. Phase composition of ceramics in systems with oxides of rare-earth elements, manganese, and titanium. Radiochemistry. 2007;49(4):346–53.
35. Lumpkin GR. Alpha-decay damage and aqueous durability of actinide host phases in natural systems. J Nucl Mater. 2001;289(1–2):136–66.
36. McAdam D, Geil G. Rate of oxidation of typical nonferrous metals as determined by interference colors of oxide films. J Res Natl Bur Stand. 1942;28(5):593.
37. Wood GC. High-temperature oxidation of alloys. Oxid Met. 1970;2(1):11–57.

SUPPORTING INFORMATION

Additional supporting information may be found in the online version of the article at the publisher's website.

How to cite this article: Dayal P, Farzana R, Zhang Y, Lumpkin GR, Holmes R, Triani G, Gregg DJ. Profiling hot isostatically pressed canister–wasteform interaction for Pu-bearing zirconolite-rich wasteforms. J Am Ceram Soc. 2022;105:5359–5372. https://doi.org/10.1111/jace.18458